Biomaterials Science

Poly-ion complex micelle effectively delivers CoA-conjugated CPT1A inhibitors to modulate lipid metabolism in brain cells

Journal:	*Biomaterials Science*
Manuscript ID	BM-ART-05-2021-000689.R1
Article Type:	Paper
Date Submitted by the Author:	22-Jun-2021

Complete List of Authors:	Paraiso, West; Kawasaki Institute of Industrial Promotion, Innovation Center of NanoMedicine (iCONM) Garcia-Chica, Jesús ; Universitat Internacional de Catalunya, Basic Sciences Department; Universitat de Barcelona, Department of Inorganic and Organic Chemistry; Universitat de Barcelona, Department of Biochemistry and Physiology Ariza, Xavier; Universitat de Barcelona, Química Orgánica Zagmutt, Sebastián ; Universitat Internacional de Cataluna, Spain, Basic Sciences Fukushima, Shigeto ; Kawasaki Institute of Industrial Promotion, Innovation Center of NanoMedicine (iCONM) Garcia Gomez, Jordi; Universitat de Barcelona, Química Orgánica Mochida, Yuki; Kawasaki Institute of Industrial Promotion, Innovation Center of NanoMedicine (iCONM) Serra, Dolors; Universitat de Barcelona, Departament de Bioquímica i Biologia Molecular Herrero, Laura; Universitat de Barcelona, Departament de Bioquímica i Biologia Molecular Kinoh, Hiroaki; Kawasaki Institute of Industrial Promotion, Innovation Center of NanoMedicine (iCONM) Casals, Nuria; Universitat Internacional de Cataluna, Spain Kataoka, Kazunori; Kawasaki Institute of Industrial Promotion, Innovation Center of NanoMedicine (iCONM); The University of Tokyo, Institute for Future Initiatives Rodriguez-Rodriguez, Rosalia; Universitat Internacional de Catalunya Quader, Sabina; Kawasaki Institute of Industrial Promotion, Innovation Center of NanoMedicine (iCONM)

Poly-ion complex micelle effectively delivers CoA-conjugated CPT1A inhibitors to modulate lipid metabolism in brain cells

West Kristian D. Paraiso[1], Jesús Garcia-Chica[2,3,4], Xavier Ariza[3,5], Sebastián Zagmutt[2], Shigeto Fukushima[1], Jordi Garcia[3,5], Yuki Mochida[1], Dolors Serra[4,5], Laura Herrero[4,5], Hiroaki Kinoh[1], Núria Casals[2,5], Kazunori Kataoka[1,6], Rosalía Rodríguez-Rodríguez[2,*], and Sabina Quader[1,*]

[1]Innovation Center of Nanomedicine, Kawasaki Institute of Industrial Promotion, Kawasaki, Kanagawa 210-0821 Japan

[2]Basic Sciences Department, Faculty of Medicine and Health Sciences, Universitat Internacional de Catalunya, Sant Cugat del Vallès, E-08195 Spain.

[3]Department of Inorganic and Organic Chemistry, Faculty of Chemistry, Institut de Biomedicina de la Universitat de Barcelona (IBUB), Universitat de Barcelona, Barcelona, E-08028 Spain.

[4]Department of Biochemistry and Physiology, School of Pharmacy and Food Sciences, Institut de Biomedicina de la Universitat de Barcelona (IBUB), Universitat de Barcelona, Barcelona, E-08028 Spain.

[5]Centro de Investigación Biomédica en Red de Fisiopatología de la Obesidad y la Nutrición (CIBEROBN), Instituto de Salud Carlos III, Madrid, E-28029 Spain.

[6]Institute for Future Initiatives, The University of Tokyo, Tokyo 113-0033 Japan.

***Corresponding authors**: Rosalía Rodríguez-Rodríguez (rrodriguez@uic.es) (Tel. +34-935-042-002) and Sabina Quader (sabina-q@kawasaki-net.ne.jp) (Tel. +81-44-589-5920)

ABSTRACT

Carnitine palmitoyltransferase 1A (CPT1A) is a central player in lipid metabolism, catalyzing the first committed step to fatty acid oxidation (FAO). Inhibiting CPT1A, especially in the brain, can have several pharmacological benefits, such as in obesity and brain cancer. C75-CoA is a strong competitive inhibitor to CPT1A. However, due to its negatively-charged nature, it has low cellular permeability. Herein, we report the use of poly-ion complex (PIC) micelles to deliver the specific CPT1A inhibitors, (±)-, (+)-, and (–)-C75-CoA into U87MG glioma cells and GT1-7 neurons. PIC micelles were formed through charge-neutralization of the cargo with the cationic side chain of PEG-poly{*N*-[*N'*-(2-aminoethyl)-2-aminoethyl]aspartamide} (PEG-PAsp(DET)), forming particles with 55 to 65-nm diameter. Upon short-term incubation with cells, the micelle-encapsulated CPT1A inhibitors resulted in up to 5-fold reduction of ATP synthesis compared to the free drug, without an apparent decline in cell viability. Micelle treatment showed a discernible decrease in ^{14}C-palmitate oxidation into CO_2 and acid-soluble metabolites, confirming that the substantial lowering of ATP production has resulted from FAO inhibition. Micelle treatment also diminished IC_{50} by 2 to 4-fold over the free drug-treated U87MG after long-term incubation. To measure cellular uptake of these CoA-adduct loaded PIC micelles, we synthesized a fluorescent CoA derivative and prepared Fluor-CoA micelle which showed efficient internalization in the cell lines, both in 2D and 3D culture models, especially in neurons where uptake reached up to 3-fold over the free dye. Our results starkly demonstrate that the PIC micelle is a promising delivery platform for anionic inhibitors of CPT1A in glioma cells and neurons, laying the groundwork for future research or clinical applications.

1. INTRODUCTION

Lipids, which include triglycerides, phospholipids, steroids, and other fat-soluble biological molecules, are important elements of the brain's structure and function, where they constitute 50% of its dry weight [1,2]. Among these, fatty acids (FAs) function as energy source, lipid membrane component, as well as starting material for signaling molecules [3]. Carnitine palmitoyltransferase 1 (CPT1) is an enzyme that catalyzes the rate-limiting step in fatty acid oxidation (FAO) – transesterification of LCFA-CoA (long-chain fatty acid-coenzyme A) and carnitine to form CoA and LCFA-carnitine esters. The resulting LCFA-carnitine can then be transported across membranes for further metabolism [4]. In mammals, there are three different CPT1 isoforms: CPT1A, which is the most ubiquitous isoform and highly expressed in the liver, kidney, and pancreas, but also astrocytes and neurons; CPT1B, which is expressed mainly in muscle and brown adipose tissue; and CPT1C, which is found exclusively in neurons and has residual CPT1 activity [5].

The CPT1 system is pivotal for the regulation of FA metabolism in most of the tissues. In the brain, particularly in hypothalamic neurons, CPT1A has been revealed as a potential target against obesity [4,6]. Accordingly, knockdown and pharmacological inhibition of CPT1A in the hypothalamus contributes to reduced food intake in rodents because of the accumulation of LCFA-CoA in the neurons [7,8]. This is thought to be a satiety signal as it precedes reduced expression of orexigenic (feeding-promoting) proteins, leading to reduced food intake [9,10], making it an appealing target for obesity. In addition to hypothalamic neurons for the regulation of energy homeostasis, CPT1A is crucial to the survival of certain cancer types, including brain cancer. Glioblastoma (GBM) in particular, has been linked with increased CPT1A expression and FA metabolism alterations. Importantly, this elevated expression of CPT1A is a very common event (90-95% cases) among human diffuse gliomas [11–13]. CPT1A-expressing tumor cells show increased FAO, promoting survival in conditions of metabolic stress like glucose deprivation and hypoxia [14]. While tumor molecular heterogeneity is an emerging critical concern in oncology, homogeneous elevated expression of CPT1A in GBM is indeed an attractive molecular target for its therapy.

Several pharmacological inhibitors of CPT1A, which act by competing with the natural inhibitor malonyl-CoA, have been investigated [15]. Examples include etomoxir (ETO) and (±)-C75, which are converted to their CoA derivatives and act on CPT1A[16,17], leading to decreased

body weight and food intake in rodents [16,17]. However, ETO was deemed too toxic for clinical use, exemplified by causing severe hepatotoxicity as a side effect [18,19].

The more promising compound is (±)-C75 (4-methylene-2-octyl-5-oxotetrahydrofuran-3-carboxylic acid). It is converted intracellularly by endogenous acyl-CoA synthetase to its CoA adduct, (±)-C75-CoA, a strong competitive inhibitor to CPT1A [16]. Its systemic administration in rats led to food intake decline and body weight decrease, as the drug was shown to cross the BBB and get converted to (±)-C75-CoA in the ARC hypothalamic nucleus [17,20]. Makowski *et al* [8] performed the stereoselective synthesis of (+)-C75 [(2*R*,3*S*) isomer] and (–)-C75 [(2*S*,3*R*) isomer] to explain their differential pharmacological activities. (+)-C75 was found to be an anorectic by inhibiting CPT1 activity after conversion to (+)-C75-CoA. On the other hand, the effect of (–)-C75 in CPT1A activity is indirect, acting via FAS inhibition driving an increase in malonyl-CoA levels, which is the physiological inhibitor of CPT1. In addition, the effects of (–)-C75 without CoA adduct on food intake were negligible, but show antitumoral effects in several cell lines [8]. The presence of the CoA adduct in C75 is therefore crucial in exerting selective inhibitory effect on CPT1 while limiting off-target effect on FAS , but it considerably reduces the uptake of the drug into the target cell. Therefore, strategies to deliver C75 derivatives with intact CoA adduct into the target cells are needed. Additionally, since brain CPT1 is implicated in both cancer and obesity, the administration of (±)-C75-CoA and its enantio-separated CoA forms into specific brain cells presents a novel therapeutic strategy to treat both diseases.

The chemical structure of (±)-C75-CoA presents challenges to cellular entry. It is a small, polar, and charged metabolite, having low permeability across the cell membrane [21], consequently needing a delivery system for intracellular transport. With its phosphate groups ionized at physiological pH, its anionic state, together with its long aliphatic side-chain enables CoA to interact with cation-conjugated polymers through a combination of electrostatic and hydrophobic interactions [22]. Therefore, forming a poly-ion complex (PIC) micelle with (±)-C75-CoA is a sound approach in designing a delivery system since this neutralizes the overall negative charge that would hinder its cellular entry. Although PIC micelles are well used for various nucleic acid-based macromolecular cargoes such as plasmid DNA, mRNA, siRNA, and anti-sense oligonucleotides (ASOs) [23–25], applications for small, ionic molecule delivery [26] are relatively scarce.

The cationic polymer used is PEG-poly{*N*-[*N'*-(2-aminoethyl)-2-aminoethyl]aspartamide} (PEG-PAsp(DET)), which has a monoprotonated side chain at pH 7.4, at which point it only causes minimal membrane destabilization. At pH 5.5, the side chain becomes diprotonated, selectively destabilizing the endosomal membrane once inside the cell, enabling less toxic gene transfer into cells [27,28]. This system has been used for mRNA transfection into neurons [29] as well as astrocytes and oligodendrocytes [30], making it an excellent candidate for (±)-C75-CoA delivery. We have successfully prepared PIC micelles from PEG-PAsp(DET) which encapsulated (±)-C75-CoA and its enantio-separated forms, potentiating the opportunity to study their biological activity on LCFA metabolism defying the cellular entry limitation. Accordingly, the micelles were tested on two brain-derived cell lines, U87MG human glioma cells and GT1-7 murine hypothalamic neurons, which revealed that FAO and ATP synthesis were successfully inhibited in both. Using a model particle encapsulating a fluorescent CoA derivative, we were also able to demonstrate that the PIC micelle is efficiently taken up by the cells and both in 2D and 3D culture models. This paper is the first report to describe the delivery of CoA-conjugated CPT1A inhibitors using PIC micelles to target CPT1A and modulate lipid metabolism in glioma cells and neurons.

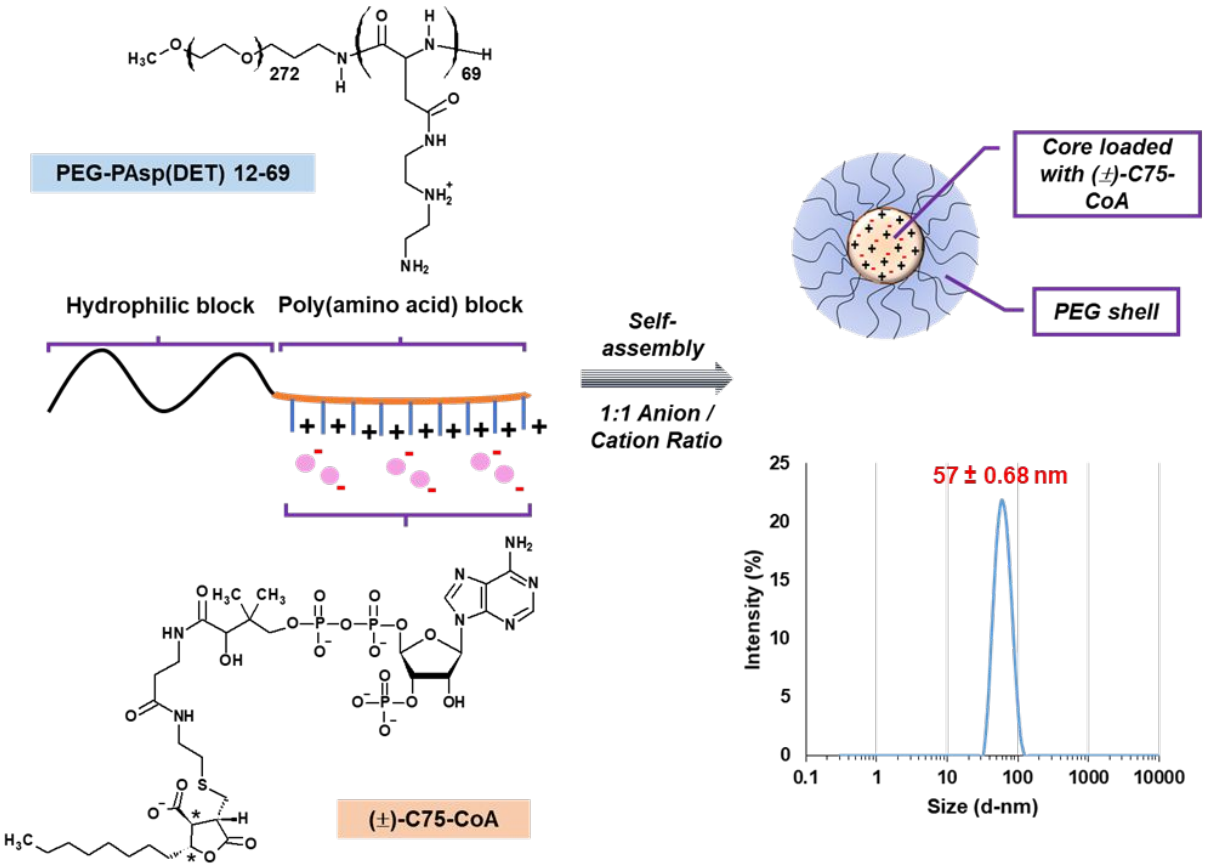

Figure 1. Schematic of a poly-ion complex (PIC) micelle formation of (±)-C75-CoA with PEG-PAsp(DET), including its size distribution profile (hydrodynamic size *versus* intensity %).

2. RESULTS AND DISCUSSION

2.1 Preparation of C75-CoA micelles

The preparation of (±)-C75-CoA was carried out as previously described [17] (see detailed information in **ESI†**). Enantioselective syntheses of (+)-C75 [(2*R*,3*S*) isomer] and (–)-C75 [(2*S*,3*R*) isomer] were performed by using enantiomeric chiral auxiliaries also as previously reported [8] (**Figure S1, ESI†**). (±)-C75-CoA were formed by nucleophilic addition to the α,β-unsaturation of (±)-C75 by the ─SH group of CoA. We confirmed the synthesis by comparing the ^{1}H NMR and HPLC profiles of the starting materials and product (**Figure S2, ESI†**). PEG-PAsp(DET) was prepared by anionic ring-opening polymerization of benzyl-L-aspartate *N*-carboxyanhydride (BLA-NCA) initiated from the terminal ─NH_2 group of CH_3O-PEG-NH_2 (MW 12,000) to form CH_3O-PEG-*b*-poly(β-benzyl-L-aspartate) (PEG-PBLA), and then subsequent aminolysis with diethylenetriamine (DET) (**Figure S3, ESI†**). The degrees of polymerization (DP) and substitution (DS) were measured from the ^{1}H NMR spectra. Using the proton peak intensity ratio of the PEG methylene protons (δ = 3.4-3.6 ppm) to the aromatic ring protons (δ = 7.1-7.5 ppm) in the polypeptide side chain of PBLA, DP was calculated to be 69. After aminolysis, the same PEG methylene protons were then compared with all the methylene protons in the DET side chains (δ = 2.7-3.6 ppm), and the DS was found to be 63.

The aqueous solutions of (±)-C75-CoA and PEG-PAsp(DET) were mixed in a 1:1 anion/cation (A/C) ratio, defined as the ratio between the overall anionic charge imparted by the phosphate and carboxylate groups in (±)-C75-CoA and the overall cationic charge given by the protonated secondary amines in PEG-PAsp(DET). We diluted the solutions using 10 mM phosphate buffer (PB) pH 7.4 to give 57-nm PIC micelles with a unimodal size profile and narrow polydispersity (PdI). The 1:1 A/C ratio was selected based on the optimal physicochemical properties obtained with this micelle, mainly the smallest micellar size and lowest PdI value **(Figure S4, ESI†)**. The zeta potential (ZP) was also close to neutral (**Figure 1, Table 1**). At pH 7.4, around 51% of the aminoethylene units in the PEG-PAsp(DET) side chain are protonated [27], this imparts a cationic charge to the block co-polymer for neutralizing the negative charge of the anionic cargo, forming PIC micelles. The PEG chain of the polymer (MW 12,000) was also crucial in

imparting these measured physicochemical properties, decreasing aggregation tendency and maintaining a neutral surface charge [23]. Transmission electron microscopy (TEM) revealed that (±)-C75-CoA micelles are spherical in shape and possess a core size of 31 nm with a unimodal size distribution **(Figure S5, ESI†)**. The core size of the micelle does not include the PEG outer shell, hence it is smaller than the hydrodynamic diameter obtained using DLS. Size and PEGylation are important considerations for brain-targeted nanoparticles (NPs). NP diffusion in the brain is affected by the finite width of the brain extracellular space (ECS) and pores in the extracellular matrix (ECM) [31]. When surface PEG density is sufficiently high, 114-nm NPs can diffuse effectively in human and rodent brains [32]. This was corroborated in subsequent literature, and now ECS widths are estimated to be 80-220 nm in diameter while pores are around 100 nm [33–35]. Increased PEG surface density is also shown to restrain non-specific cellular uptake of NPs [36], which removes another impediment for diffusion. The size of (±)-C75-CoA micelle is therefore ideal for moving through the brain parenchyma.

(+)- and (–)-C75-CoA were synthesized from the same procedure as (±)-C75-CoA and their corresponding micelles were also successfully prepared, with near-similar physicochemical properties (**Table 1**). Additionally, micelles loaded with other CoA derivatives were prepared in order to confirm the applicability of the delivery system to molecules with similar structures. First, we used commercially available palmitoyl-CoA since its hydrophobic tail resembled that of (±)-C75 and their molecular weights were also numerically close. Micelle formation with palmitoyl-CoA was indeed observed based on DLS measurements. However, when we used CoA (767.5 g/mol) or malonyl-CoA (853.6 g/mol), micelle formation was not detected. The probable reasons are that their MWs were much smaller from (±)-C75-CoA and that they did not possess the characteristic hydrophobic moieties, despite having the phosphate groups necessary for PIC formation. This indicates that hydrophobicity was to some degree a part of the driving force for micelle formation. To determine the percentage of (±)-C75-CoA loaded inside the micelle, ultracentrifugation was used to remove the unencapsulated free drug. The ratio of the drug concentration in the upper fraction of the filter and the total drug added in the micelle preparation was calculated. From this, we ascertained that (±)-, (+)-, and (–)-C75-CoA micelles all have high drug encapsulation rates (above 80%). The ionic interaction between the drug and polymer was further confirmed by the statistically significant decrease in scattering light intensity and % encapsulation when (±)-C75-CoA micelle was mixed with concentrated salt solutions (0.5 or 1 M NaCl) (**Figure S6**, **ESI†**). Formation of PIC is driven primarily by the liberation of counterions [23] which is prompted when the cationic DET side chain and

anionic drug paired up, leading to a large entropic gain. The increased NaCl concentration apparently reduced this entropic gain, which resulted in the destabilization of the PIC structure.

Cargo		Micelle			
Molecule	**MW (g/mol)**	**Size (d-nm)**	**Polydispersity**	**Zeta potential (mV)**	**Encapsulation (%)**
(±)-C75-CoA	1004	56.7 ± 0.68	0.055 ± 0.0037	-0.29 ± 1.98	84.2 ± 0.52
(+)-C75-CoA	1004	63.5 ± 1.45	0.054 ± 0.0082	-0.68 ± 2.25	82.2 ± 0.01
(–)-C75-CoA	1004	55.0 ± 0.38	0.024 ± 0.0232	0.17 ± 2.62	87.3 ± 0.03
Palmitoyl-CoA	1005.9	59.5 ± 0.69	0.022 ± 0.0017	2.37 ± 0.85	66. 8 ± 0.05
Fluorescein-CoA	1175.8	56.9 ± 0.16	0.037 ± 0.0070	0.38 ± 1.46	94.3 ± 0.18

Table 1. Physicochemical characteristics of (±)-C75-CoA, Palmitoyl-CoA and Fluorescein-CoA micelles. Experiments were performed in triplicate, with values expressed as mean ± SD.

Next, to evaluate its long-term stability in cold storage, the change in micelle characteristics was monitored every 7 days for a total of 28 days during storage at 4 °C (**Figure 2**). The purpose of this experiment was to ensure that micelles prepared in advance can still be used in biological assays after a few days of storage enabling easy and efficient reproducibility of experimental results. One-way analysis of variance (ANOVA) revealed apparent linear relationships between each physicochemical parameter and incubation time. We observed micelle size to increase slightly with time ($R^2 = 0.9609$) (**Figure 2 a**). This increase in size was accompanied by a steady increase in scattering light intensity ($R^2 = 0.9984$) (**Figure 2 b**) as expected, indicating that no apparent decrease in particle concentration occurred. There was also no apparent change in PdI throughout the observation period (**Figure 2 c**). The size profile remained monodisperse, as the PdI remained well below 0.1, which was narrow. ZP stayed close to neutral all throughout the observation period, despite a weak increase associated with time ($R^2 = 0.7432$) (**Figure 2 d**). However, there was no significant change between the initial

and final values. Overall, despite the tendency to gradually change over time, it is reasonable to conclude that micelle integrity was maintained for 28 days in storage at 4 °C.

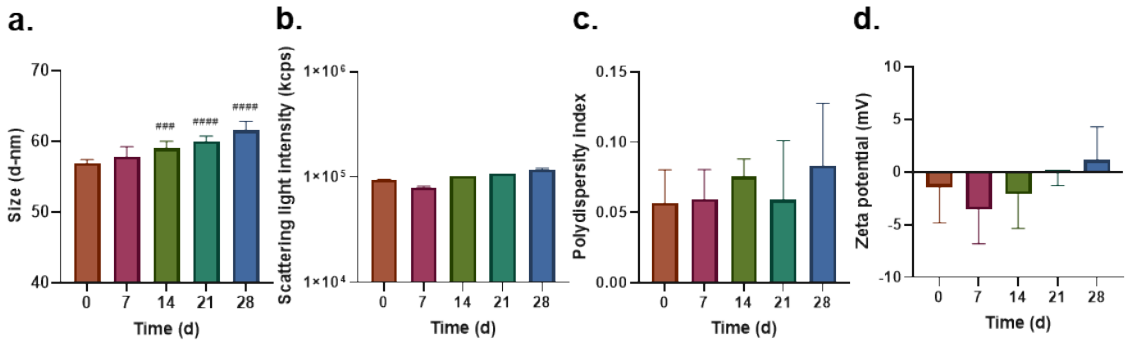

Figure 2. Long term stability studies of (±)-C75-CoA micelle, including measuring changes in physicochemical properties over 28 days in storage at 4 °C: size (a), scattering light intensity (b), polydispersity (c), and zeta potential (d). Experiments were performed in triplicate (values expressed in mean ± SD) and linear relationships were established using ANOVA. Comparison of means among treatment groups were done using ANOVA (with Tukey's test as post-hoc analysis; ###P<0.001, ####P<0.0001 *versus* day 0 of measurement).

PIC micelles from charged block copolymers exhibit critical association behavior [24], which predicts the stability of a drug delivery system in an environment where it is highly diluted. Using static light scattering (SLS), we measured the scattered light intensity of diluted PIC micelle solutions as expressed by the following equation:

$$\frac{Kc}{\Delta R(\theta)} = \frac{1}{M_{w,\,app}} + 2A_2c$$

where $M_{w,\,app}$ is the apparent molecular weight of the micelle, A_2 is the second virial coefficient, c is the concentration of the micelle solution, $\Delta R(\theta)$ is the difference between the Rayleigh ratio of the micelle solution and the solvent (10 mM phosphate buffer), and K, the Debye constant, is calculated using $4\pi^2 n^2 (\frac{dn}{dc})^2 / \lambda^4 N_A$ (where N_A is Avogadro's number).

Abrupt changes in the $Kc/\Delta R(\theta)$ values in a Debye plot reveal changes in molecular weight of micelles. When these measurements are near-constant at a certain concentration range, micelle integrity is maintained. At lower (±)-C75-CoA micelle concentrations (0.005 to 0.1 mg/mL), a sharp decrease in $Kc/\Delta R(\theta)$ was apparent (**Figure 3**). However, at higher concentrations (0.15 to 1.0 mg/mL), $Kc/\Delta R(\theta)$ values became nearly constant. The point of intersection of two straight lines drawn from the lower and higher concentration range give the critical association concentration (CAC) of the micelle, which is 0.09 mg/mL. Thus, given its low CAC value, the

micelle formed from PEG-PAsp(DET) is expected to have excellent stability in dilute systems. The equivalent drug concentration at CAC is 0.03 mM (±)-C75-CoA. Concentrations much higher than this were employed in subsequent biological experiments.

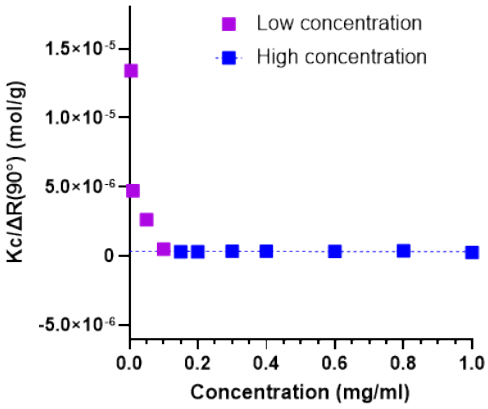

Figure 3. Critical association behavior of (±)-C75-CoA micelle. Gray squares indicate lower micelle concentrations while black squares indicate higher micelle concentrations. The known Rayleigh ratio of toluene used as calibration standard and the detection angle θ = 90° was used. Measurements were carried out at 25 °C.

2.2 Inhibition of fatty acid metabolism

2.2.1 ATP synthesis

LCFAs need to enter the mitochondria to undergo β-oxidation. They are first esterified into the LCFA-CoA form and subsequently shuttled into the mitochondria by CPT1A (**Figure 4 a**). Upon entry, the LCFA-CoA undergoes β-oxidation to form several acetyl-CoA molecules, which then enters the Krebs cycle. Acetyl-CoA is eventually degraded into CO_2, and in the process produces NADH, which enters the electron transport chain (ETC) to finally yield ATP [37,38]. By this pathway, FAO inhibition is known to impair ATP production. We examined whether C75-CoA will show this effect by measuring ATP concentration in cells after incubation with free and micellar C75-CoA (**Figure 4 b-c**) for 45 minutes. In general, the micelle effect is well-pronounced as the ATP concentrations from micelle-treated cells are significantly lower than those from free drug-treated groups. This suggests that the effective delivery of C75-CoA inside the cells led to a higher concentration of the compound reaching the mitochondria, further steering into a substantial inhibition of FAO by the nano-encapsulated drugs.

U87MG is the most widely used cell line for human glioma research [39]. It was also reported to express CPT1A [12], making it an appropriate model for our subsequent experiments. For U87MG, neither ETO nor the free drugs with CoA adduct, were able to effectively reduce ATP levels (**Figure 4 b**). Nevertheless, cells treated with (±)-, (–)- and (+)-C75-CoA micelles showed significant reduction in ATP levels compared to their corresponding non-encapsulated drugs. This ATP lowering effect is particularly appreciated with (–)-C75-CoA micelle, which was the most effective compared to all other groups. Although the lack of effect of ETO in ATP levels did not correlate with previous publications [40,41] , we observed a reduction in FAO assay with ETO in U87MG (**Figure 5 c**), confirming the inhibitory effect of this drug on mitochondrial metabolism, although the dosage-dependent off-target effects attributed to ETO could explain the result in ATP levels [42] .

GT1-7 is an immortalized murine hypothalamic neuronal cell line which is used in endocrinology and metabolism studies [43]. It was also reported to express CPT1A [44] and since it is in our interest to measure its inhibition in the hypothalamus, this cell line is an appropriate *in vitro* model. ATP levels in GT1-7 were discernibly reduced in response to ETO and by the free (±)- and (–)-C75-CoA derivatives, but no changes were observed in the (+)-C75-CoA-treated group (**Figure 4 c**). Drug encapsulation led to a statistical enhancement in ATP reduction induced by both (+)- and (–)-C75-CoA forms. As shown in U87MG, (–)-C75-CoA micelle was still most effective in reducing ATP among all treatment groups including ETO.
A concurrent cell viability assay confirmed that the treatments in both U87MG and GT1-7 cells did not cause any apparent cell death, compared with the non-treated group (**Figure 4 d-e**). This highlights one of the advantages of the delivery system that we used, since PEG-PAsp(DET) causes only minimal toxicity [27]. Although other cationic polymers like poly-(L-lysine) and poly(ethylenimine) (PEI) are well-used to deliver anionic molecules, their toxicity upon micellar disassembly limits their biological applications [45]. Overall, our results verify that for both cell types, the micelles were more successful in reducing ATP synthesis as compared to the free drugs, without causing excessive cell death.

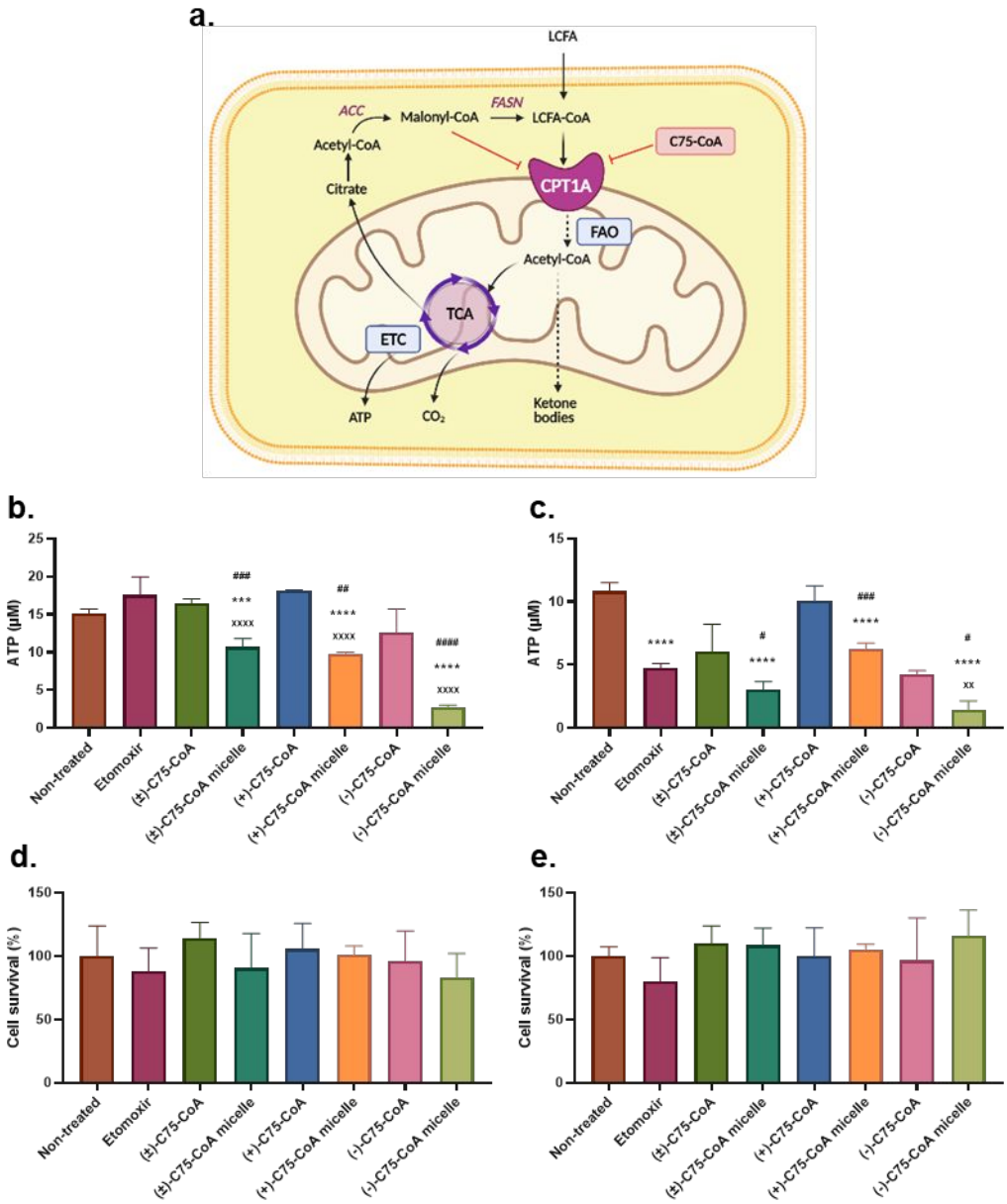

Figure 4. Illustration of ATP generation from LCFA metabolism (a). Levels of ATP produced by U87MG (b) and GT1-7 (c) after treatment with FAO inhibitors. Simultaneous Calcein AM cell viability assay for U87MG (d) and GT1-7 (e) using the same conditions and treatments as ATP assay. Experiments were performed in quadruplicates (values expressed in mean ± SD) and comparison of means among treatment groups were done using ANOVA (with Tukey's test as post-hoc analysis; ***P<0.001, ****P<0.0001 *versus* non-treated cells; ^{xx}P<0.01, ^{xxxx}P<0.0001 *versus* ETO; $^{\#}$P<0.05, $^{\#\#}$P<0.01, $^{\#\#\#}$P<0.001, $^{\#\#\#\#}$P<0.0001 *versus* the corresponding free form of C75-CoA). Concentrations of all inhibitors used = 0.5 mM.

2.2.2 FAO assay

Palmitate oxidation in both U87MG and GT1-7 cells was evaluated in terms of: oxidation to CO_2 (**Figure 5 a & d**), conversion to acid-soluble products (ASPs) (**Figure 5 b & e**) and total FAO rate calculated as the sum of ASP plus CO_2 oxidation (**Figure 5 c & f**). The final fate of palmitate oxidation in both cell types was significantly different. In particular, most of palmitate oxidation levels measured in U87MG cells come from ASPs (ranging 7.5 nmol/mg

prot/h), with minimal contribution of oxidation to CO_2 (ranging 0.1 nmol/mg prot/h), whereas GT1-7 cell lines showed more equitable contribution of palmitate oxidation to ASPs and CO_2 total FAO. The differences in palmitate oxidation fate between GBM or neuronal cell lines agree with previous publications indicating the different metabolic profile of both cell types [12,40,46,47].

In U87MG cells, ETO effectively reduced FAO in terms of both CO_2 and ASP (**Figure 5 a-c**), since ASP oxidation was the main pathway contributing to total reduction of FAO. In contrast, the free forms of C75-CoA were unable to modify these oxidation parameters compared to non-treated cells. Micelles of the three forms of C75-CoA led to a substantial attenuation of total FA oxidation (**Figure 5 c**), reaching similar levels to ETO-treated cells. These changes were due to palmitate oxidation to ASP (**Figure 5 b**), probably reducing the generation of TCA intermediary metabolites and ketone bodies crucial for GBM cell proliferation [12,40]. Similar levels of FAO attenuation were reached in (±)-, (+)- and (–)-C75-CoA micelle-treated U87MG cells (**Figure 5 c**).

In GT1-7, ETO was also able to reduce FAO, whereas it remained unchanged after treatment with the free C75-CoA forms, in line with previous results (**Figure 5 d-f**). The micelle forms of C75-CoA derivatives induced a statistically significant attenuation in total FAO, with the contribution of both palmitate fates, to CO_2 and ASP, being similar to the total oxidation of FA (**Figure 5 d-f**). Cells treated with (±)-C75-CoA micelle showed the highest reduction in FAO compared to non-treated conditions, reaching similar levels to those induced by ETO (**Figure 5 c**).

Altogether, our results indicate that the delivery of C75-CoA derivatives using a PIC micelle resulted in a substantial improvement in FAO inhibition by these drugs in both U87MG and GT1-7 cell lines. We have also evidenced the differential contribution of either CO_2 or ASPs to FA oxidation in both cell lines, in agreement with the literature. Considering the recently identified role of FAO as a metabolic node in the aggressive phenotype of glioma cell lines [40,41], and the significant role of FA oxidation and CPT1 in neuronal metabolism and survival [44,47], the improved FAO inhibition showed by these micelles indicate the potential of these nanoparticles to modify brain metabolism in associated diseases such as cancer.

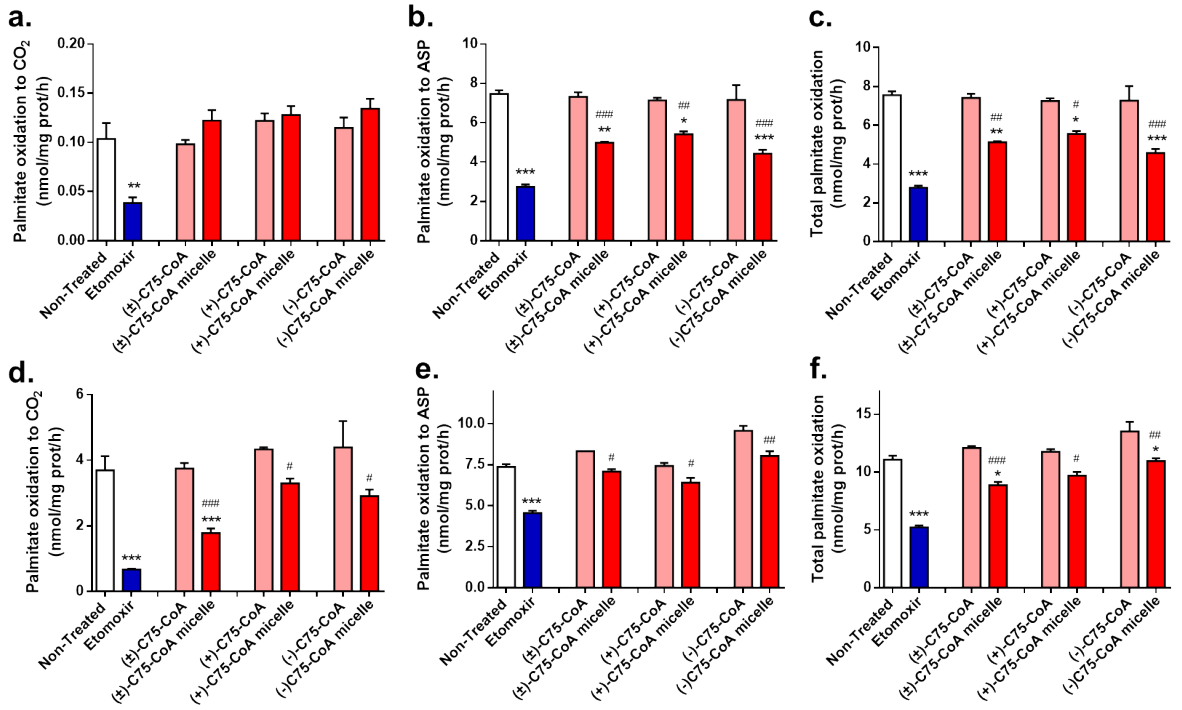

Figure 5. FAO oxidation in U87MG (a-c) and GT1-7 (d-f) cells after treatment with C75-CoA derivatives in free form or nano-encapsulated in micelles. ETO was used as positive control of FAO inhibition. FAO is represented as palmitate oxidation to CO_2 (a, d), ASP (b, e), and total palmitate oxidation (CO_2 + ASP; c, f). Results are the mean ± SD of two independent experiments performed by biological triplicates (n=5-6 samples per condition). Comparison of means were done using ANOVA followed by Tukey's comparison test; *P<0.05, **P<0.01, ***P<0.001 *versus* non-treated cells; #P<0.05, ##P<0.01, ###P<0.001 *versus* the corresponding form of C75-CoA. Concentrations of all inhibitors used = 1 mM.

2.3 Cytotoxicity of C75-CoA micelles

Since GBM cells overexpress CPT1A [11] to increase their chances of survival, inhibiting this enzyme would negatively affect their proliferation. We incubated free and micellar C75-CoA with U87MG for 72 h, with ETO as a comparison drug. The drug and micelle-produced responses generally followed a sigmoidal shape (**Figure 6 a-d**). C75-CoA (racemic and enantio-separated forms) is overall significantly more cytotoxic to the respective free drug (**Figure 6 e**). Notably, the mean IC_{50} of free (±)-C75-CoA was decreased 4-fold when delivered in micelle form. After 72 h, the difference between the mean IC_{50} of (±)- and (–)-C75-CoA micelles are not statistically significant, however, (+)-C75-CoA micelle is discernibly less cytotoxic than (±)-C75-CoA micelle. Free (+)-C75-CoA is less cytotoxic than ETO. On the other hand, ETO shows comparable toxicity to (±)- and (–)-C75-CoA micelles despite being a free drug, owing to other mechanisms outside of CPT1 inhibition such as production of reactive oxygen species [38,48].

Two-way ANOVA revealed that the mean IC_{50} values of all FAO inhibitors were all found to decrease with time in a linear fashion ($R^2 > 0.9$). The cytotoxicity of (±)-C75-CoA micelle was demonstrated to be more pronounced at longer incubation periods, approaching comparable values as ETO after 72 h (**Figure 6 f**). Note that decrease in cell viability is achieved only upon lengthier exposure, since the 45-min incubation in the ATP assay (**Figure 4 c**) was not enough to kill the cells. Cellular morphologies were also retained after short-term incubation with both free and micellar (±)-C75-CoA in the FAO assay (**Figure S7, ESI†**), including the neuronal and astrocytic processes for GT1-7 and U87MG, respectively. These results provide the initial evidence to support the further development of these PIC micelles as a therapeutic platform against GBM. It also shows that the delivery of (±)-C75-CoA inside the cell is important in amplifying its growth inhibitory properties. Given its anionic state, it is assumed to have limited permeability across the cell membrane [21], with the micelle state neutralizing this negative charge and promoting its transport into the cell through endocytosis.

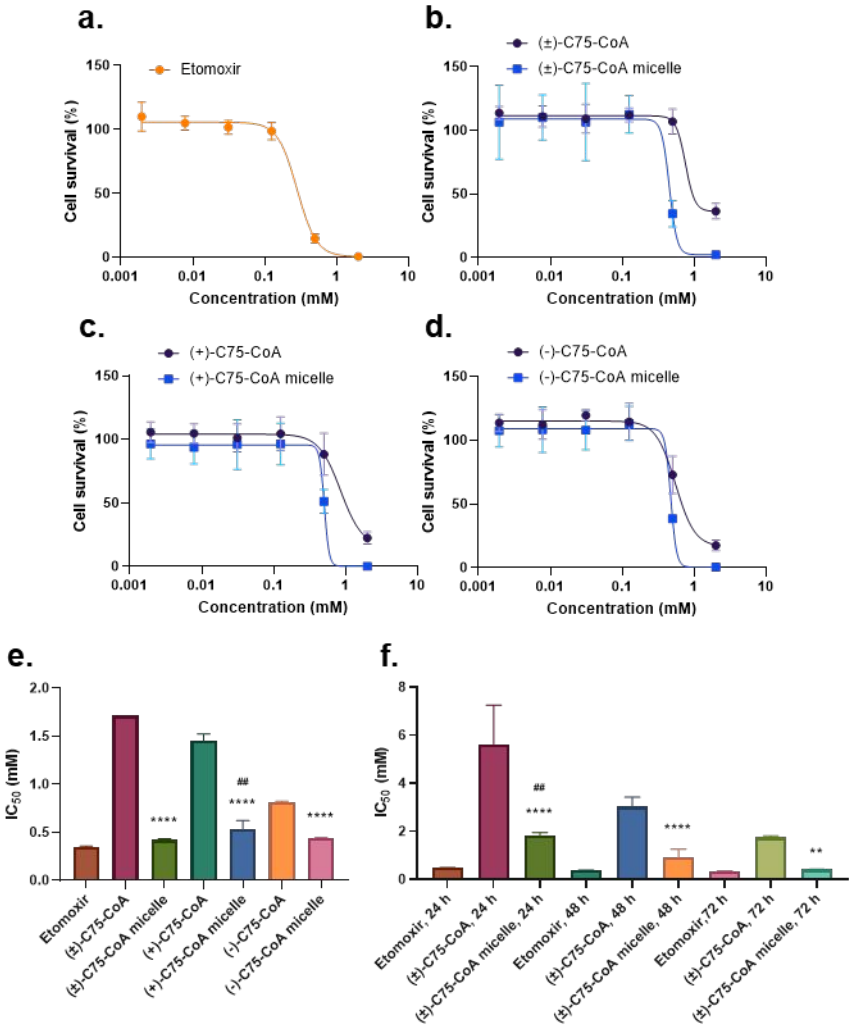

Figure 6. Cytotoxicity of FAO inhibitors on U87MG at 72 h incubation, including the dose-response curves of ETO (a) and the free *versus* micelle forms of (±)-C75-CoA (b), (+)-C75-CoA (c), and (–)-C75-CoA (d). IC_{50} of ETO, free. and micelle forms of (±)-, (+)-, and (–)-C75-CoA at 72 h incubation (e) and only for (±)-C75-CoA at 24-, 48-, and 72-h incubation periods (f). Experiments were performed in triplicates (n=4 samples per condition; values expressed in mean ± SD) and comparison of means among treatment groups were done using one-way ANOVA (with Tukey's test as post-hoc analysis; **P<0.01, ****P<0.001 *versus* the corresponding form of C75-CoA; $^{\#\#}$P<0.01 *versus* ETO).

2.4 Quantification of cellular uptake using Fluorescein-CoA encapsulated PIC micelle in 2D and 3D culture models

To confirm that PIC micelle type system facilitated cellular uptake of CoA-conjugated (±)-C75 by neutralizing the negative charges, we synthesized a fluorescein analogue of CoA (**Figure 7**; Fluorescein-CoA; herein Fluor-CoA) and encapsulated it inside the PIC micelle. Fluor-CoA was prepared by simple maleimide chemistry starting from fluorescein-5-maleimide (FAM). The resulting compound had a MW (1175.8 g/mol) close to (±)-C75-CoA (1004 g/mol), including the same number of carboxylate and phosphate groups, which therefore imparted

analogous physicochemical properties. The fluorescein moiety also imparted sufficient hydrophobic character to CoA, which is necessary for PIC micelle formation. The addition of fluorescence emission ($\lambda_{excitation}$ = 475-490 nm, $\lambda_{emission}$ = 510-520 nm) made cellular uptake studies using confocal microscopy or flow cytometry possible. The ─SH group of CoA added to the maleimide ring of FAM to give the desired product (**Figure S8 a, ESI†**), which we confirmed by comparing the ^{1}H NMR and HPLC profiles of the starting materials and product (**Figure S8 b-c, ESI†**). In the chromatogram, the Fluor-CoA peak is revealed by both the fluorescence and UV absorbance (λ_{max} of CoA) detectors. In a similar fashion to (±)-C75-CoA, the aqueous solution of Fluor-CoA was combined with PEG-PAsp(DET) in a 1:1 anion/cation ratio in 10 mM phosphate buffer (PB) pH 7.4 to give 57-nm micelles with a narrow polydispersity (**Table 1**).

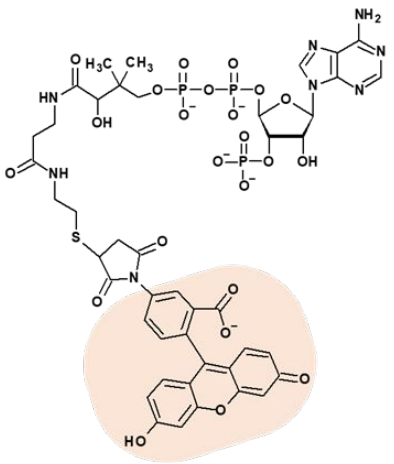

Figure 7. Structure of Fluor-CoA. The fluorescein moiety (highlighted) enables uptake evaluation using flow cytometry or confocal microscopy.

Cellular uptake in both U87MG and GT1-7 was visualized using confocal laser scanning microscopy (CLSM) and quantified using flow cytometry (**Figure 8**). We incubated the micelles with the cells at different time points (1, 3, or 6 h) and at a fixed concentration of Fluor-CoA micelle (0.25 mg/mL), which contained 0.1 mg/mL free dye. The equivalent Fluor-CoA concentration was therefore used in the free dye-treated groups. In flow cytometry, DAPI-stained dead cells were excluded in order to measure only live cells. The data we obtained included mean fluorescence intensity (MFI), to indicate extent of micelle internalization, and percentage of Fluor-CoA+ cells after gating, to quantify the % of cell population in which the free or micellar Fluor-CoA have entered.

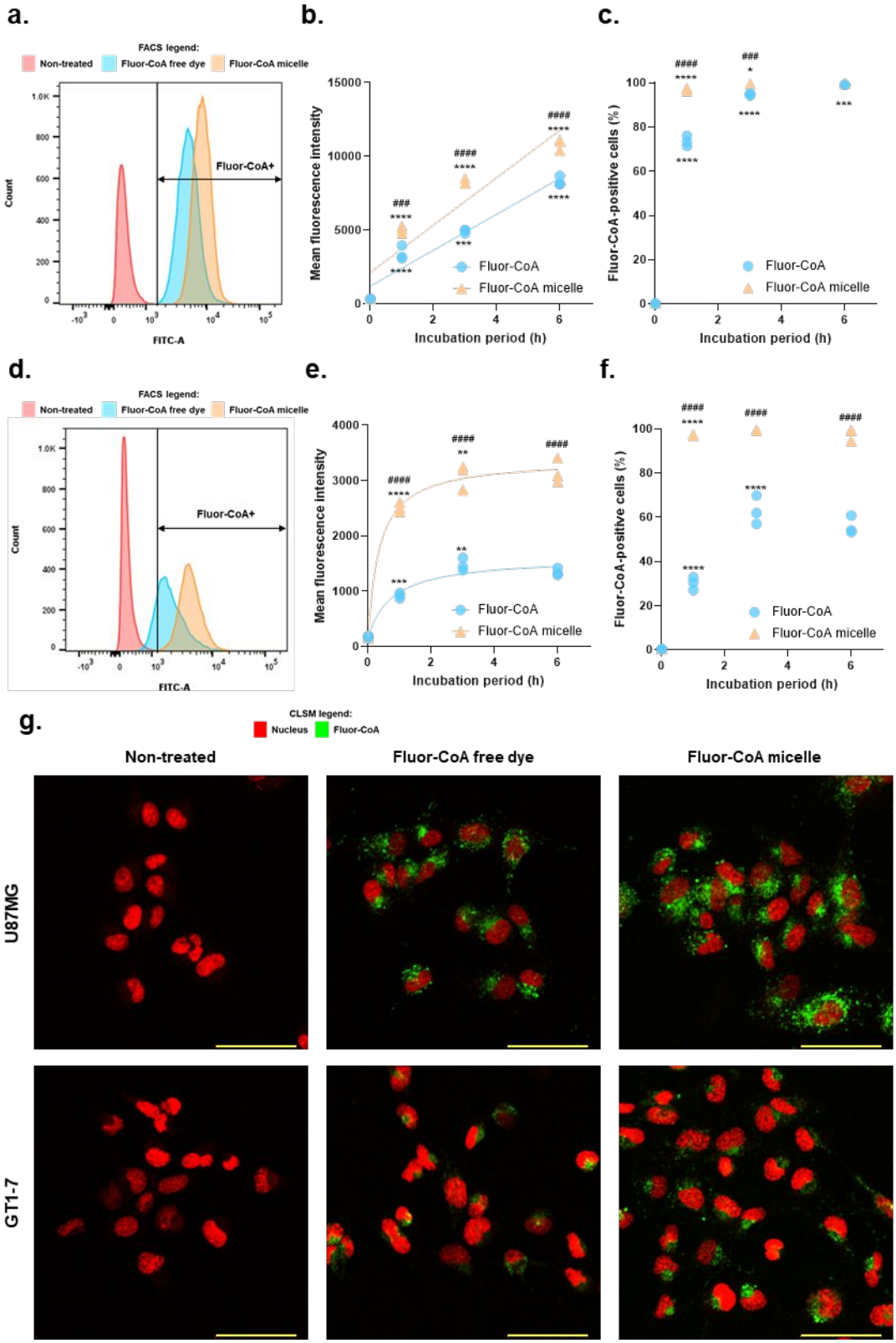

Figure 8. Analysis of cellular uptake of Fluor-CoA micelles *versus* free dye in 2D cultures using flow cytometry and confocal microscopy. U87MG data (a-c) are presented as sample histogram (a), mean fluorescence intensity (b), and percentage of Fluor-CoA-positive cells (c). GT1-7 data (d-f) are presented as sample histogram (d), mean fluorescence intensity (e), and percentage of Fluor-CoA-positive cells (f). Experiments were performed in triplicate (values expressed in mean ± SD) and comparison of means among treatment groups were done using ANOVA (with Tukey's test as post-hoc analysis; *P<0.05, **P<0.01, ***P<0.001, ****P<0.0001 *versus* measurement at preceding time point; ###P<0.001, ####P<0.0001 *versus*

corresponding free Fluor-CoA). Representative confocal microscopy images (g) of U87MG and GT1-7 after 1 h incubation with Fluor-CoA free dye and micelle. Scale bar = 50 µm, magnification 5×.

Internalization of both free dye and micelle increased with time in both cells (**Figure 8**). Mutually, micellar uptake in terms of MFI was statistically higher than free dye uptake, at all measured time points (**Figure 8 b & e**). In addition, the values for %Fluor-CoA+ cells were discernibly greater for the micelle compared to the free dye, for both cell lines (**Figure 8 c & f**). Even after 1 h of incubation, the micelles have entered more than 95% of the cells. For U87MG specifically, MFI corresponding to micelle uptake was 1.5-fold elevated, on average, compared to that of the free dye (**Figure 8 b**). We found that cellular uptake displayed a strong linear increased over time for both micelle (R^2 = 0.8708) and free dye (R^2 = 0.9394). This meant that the cells were expected to continue internalization beyond the 6-h observation period. In terms of %Fluor-CoA+ cells, free dye uptake started at only 70% (1 h) but gradually increased and eventually matched the corresponding value for the micelle at 6 h (**Figure 8 c**). However, the micelle-treated cells still produced a higher fluorescence signal, signifying that the overall amount of Fluor-CoA delivered to the cells was higher. Mo *et al* [49] has previously described the tendency of U87MG to internalize polymeric NPs at a steady linear rate up to 6 h, which supports our findings.

The difference between micellar and free Fluor-CoA uptake was more amplified in GT1-7. MFI of micelle uptake was around 2 to 3 times higher than free dye uptake through all the time points that we measured, which clearly indicated the penetration-enhancing effects of the micelle (**Figure 8 e**). In terms of %Fluor-CoA+ cells, the uptake started from 30% at 1 h, doubled at 3 h, and then plateaued (**Figure 8 f**). Unlike in U87MG, the rates of internalization did not increase in a linear fashion but fit a non-linear model called the Padé (1,1) approximant (Fluor-CoA R^2 = 0.9493; Fluor-CoA micelle R^2 = 0.9870). In addition, the free drug entered only around 60% of the cell population even at a 6-h incubation period, never quite reaching the 98% uptake that the micelle has attained after only 1 h of incubation. The saturable uptake of PEGylated polymeric micelles has previously been demonstrated for neurons by Rabanel *et al* [50] who attributed it to their limited capacity to accommodate NPs.

Multi-cellular spheroids were generated by seeding cells in low-adhesion plates and allowing them to form clusters by secreting their own ECM [51], which provides additional penetration barriers for the NPs [52], therefore more accurately modeling the *in vivo* environment as

compared to the monolayer culture. We found that micellar internalization was also 1.4- and 2-folds higher compared to the free dye in U87MG and GT1-7 spheroids, respectively (**Figure 9 a & c**). In GT1-7 spheroids, 30% of the cells have internalized the free dye, compared to the 80% which internalized the micelles (**Figure 9 d**). For U87MG, the difference of %Fluor-CoA+ cells between the free dye- and micelle-treated groups remained small but still statistically significant, similar to the 2D culture model (**Figure 9 b**).

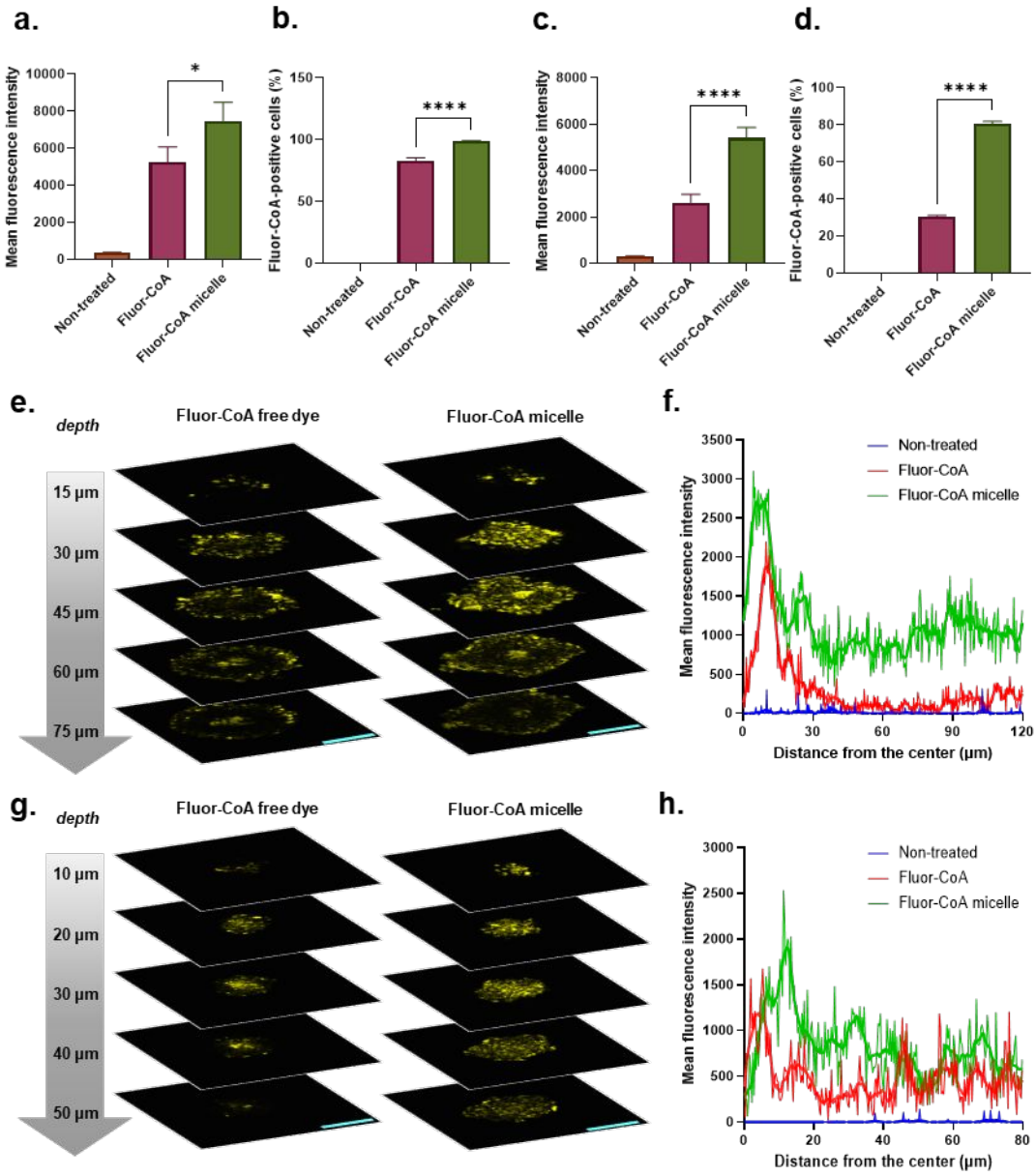

Figure 9. Analysis of cellular uptake of Fluor-CoA micelles *versus* free dye in 3D cultures using flow cytometry and confocal microscopy. FACS analysis for U87MG presented as mean fluorescence intensity (a), and percentage of Fluor-CoA+ cells (b) and for GT1-7 presented as mean fluorescence intensity (c), and percentage of Fluor-CoA+ cells (d). Experiments were performed in triplicate (values expressed in mean ± SD) and comparison of means among treatment groups were done using ANOVA (with Tukey's test as post-hoc analysis) (*p<0.05, ****p<0.0001). Representative confocal microscopy images of U87MG (e) and GT1-7 (g) spheroids taken at Z-positions. Yellow signals represent fluorescence from the FITC channel. Scale bar = 100 µm, magnification 1.2×. Radial profile of fluorescence from Fluor-CoA micelles

***versus* free dye in U87MG (f) and GT1-7 (h) spheroids. Actual fluorescence intensity as well as 10-point moving average as represented by a smoothing curve are shown. All data were taken after 3 h incubation with Fluor-CoA micelle or free dye.**

Confocal images from the periphery to the core of the spheroids show the contrasting penetration abilities between Fluor-CoA free dye and micelle (**Figure 9 e-h, Figure S9, ESI†**). For both cell lines, the peak presence of Fluor-CoA is found between 0-20 μm from the periphery. The signal steadily decreased towards the core. Generally, fluorescence intensity coming from micelle-treated spheroids are consistently higher in micelle-treated spheroids, confirming what was already shown in flow cytometry measurements: that internalization of Fluor-CoA micelles is higher than the free dye. Through the confocal images, we also demonstrated that Fluor-CoA micelles have higher penetrating ability than the free Flour-CoA. The results suggest that even in a 3D model with additional barriers, our above findings in the monolayer hold true. Additionally, this implies that the PIC micelles that we prepared are equipped to navigate through the pores of the ECM.

3. CONCLUSION

We have successfully prepared PIC micelles loaded with the CPT1A inhibitors (±)-, (+)-, and (–)-C75-CoA. The cationic block-copolymer PEG-PAsp(DET) provided a platform by neutralizing the negative charge of the cargo molecules, generating micelles with optimal physicochemical properties (55-65 nm size range and neutral surface charge) that are stable in long term storage. Through targeting CPT1A, FAO was effectively impeded, which led to overall decreased metabolism of ^{14}C-palmitate into CO_2 and acid-soluble products. We found that these results were consistent with the ATP inhibition experiments, where ATP production in both U87MG and GT1-7 was diminished up to 5-folds by the micelles, in comparison with the free drug counterparts. During these short-term incubation experiments, no apparent decrease in viability was induced by the micelles. When we assayed the cytotoxicity in glioma cells after longer incubation periods, C75-CoA micelles inhibited cell growth more discernibly compared to the free drug forms, where IC_{50} was reduced 2 to 4-folds. (±)- and (–)-C75-CoA micelles even showed comparable efficacy to the known FAO inhibitor ETO. The fluorescent dye-loaded model particle, Fluor-CoA micelle, showed a statistically increased internalization in both cell lines as well, in comparison with the free dye, reaching a 2 to 3-fold increase especially in GT1-7 neurons. Higher cellular internalization corroborated the cytotoxicity and FAO inhibition results, that delivery through PIC micelle resulted in increased cellular

concentration of the cargo, which further led to increased biological activity. Although internalization was generally time-dependent, we showed that the micellar uptake kinetics differed between the cell lines. Effective cellular entry of Fluor-CoA micelle was further confirmed in 3D spheroids derived from both cell lines, inferring the superior activity of CoA-adducts when loaded in micelles in a biological model that is transitional in complexity between standard 2D *in vitro* and diseased tissue *in vivo*. The size range and neutral surface charge of these PIC micelles, combined with their efficient penetration in 3D spheroids, imply that this platform is ideal in navigating through the brain parenchyma. This justifies further exploration of its *in vivo* properties in subsequent works. This PIC micelle has previously been reported to be effective in gene delivery to the brain including in glial cells like astrocytes and oligodendrocytes [30] as well as neurons [29]. From our data, we can compellingly conclude that uptake in neuronal and glioma cells of small anionic cargoes like Fluor-CoA and by extension, C75-CoA, is thoroughly improved by using a PIC micelle. Additionally, the advantage of using a micelle-type delivery system was more pronounced for the neurons. Drug delivery into neurons is generally more challenging compared to other cells and this is reflected in the fact that there is a lack of neuron-targeted delivery systems present in the clinic [53]. Our results contribute to the growing pool of knowledge on glioma- and neuron-targeted delivery, therefore warranting further development into effective brain therapeutics, especially those that involve the delivery of CPT1A inhibitors and other negatively-charged molecules for management of diseases where modulating lipid metabolism is a key emerging strategy.

4. MATERIALS AND METHODS

4.1 Synthesis of (±)-C75-CoA, (+)-C75-CoA and (–)-C75-CoA

The preparation of (±)-C75-CoA was carried out as previously described [17] (see detailed information in **ESI†**). Enantioselective synthesis of (+)-C75 and (–)-C75 was performed by using enantiomeric chiral auxiliaries (**Figure S1, ESI†**).

4.2 Synthesis of PEG-PAsp(DET)

The preparation of PEG-PBLA through NCA ring-opening polymerization of BLA-NCA (Chuo Kaseihin Co., Inc.) using CH_3O-PEG-NH_2 (MW 12,000; NOF Corp.) was carried out as previously reported [54]. Subsequent aminolysis of the polymer with freshly distilled DET

(TCI, cat. # D0493) was carried out also as described earlier [27,28]. See detailed information in **ESI**†.

4.3 Preparation and characterization of PIC micelles

PEG-PAsp(DET) was dissolved in 10 mM phosphate buffer pH 7.4 at 10 mg/mL concentration by overnight stirring at 4 °C. After which, the solution was passed through using 0.22-μM filter. The polymer and (±)-C75-CoA solutions were mixed in a 1:1 anion-to-cation ratio, vortexed, and then again filtered (0.22-μM) under sterile conditions prior to succeeding experiments. For DLS measurements (Zetasizer Ultra, Malvern Panalytical, Spectris plc, UK), micelle suspensions were diluted to 1 mg/mL and placed inside a ZEN2112 quartz cuvette. Light scattering data was measured using a 50-mW 532 nm DPSS laser incident beam at a detection angle of 173° with a He-Ne laser 633 nm (temperature = 25 °C). The autocorrelation function produced was analyzed through the cumulant approach. Size is expressed as the hydrodynamic diameter, which was calculated with the Stokes−Einstein equation. Attenuator selection was automated. For zeta potential measurements, micelle suspensions were introduced in a ZEN1010 HC cell, using the Smoluchowski approach. During stability studies, micelles were kept at 4 °C and measurements were repeated every 7 d for 28 d in total.

For static light scattering (SLS) measurements, Dynamic Light Scattering Photometer DLS-8000 (Otsuka Electronics, Osaka, Japan) was used. Measurements were performed using a detection angle of 90° with a He-Ne laser 633 nm at 25 °C on micelle solutions with a concentration range of 0.005 to 1 mg/mL. To measure background light scattering, the solvent phosphate buffer pH 7.4 (10 mM) was used. Calibration was performed using toluene.

Micelle morphology was observed on a Transmission Electron Microscope (JEM-2100, JEOL, Japan) operated with 120 kv acceleration voltages and approximately 60 μA beam current. The diluted micelle (1 mg/mL) was stained by mixing with uranyl acetate solution (2%, w/v) and placed on 400-mesh copper grids before drying and observation. Micelle diameter (n = 105) was measured using IC Measure version 2.0.0.245.

4.4 Quantification of drug inside PIC micelles

Micelle solutions were pipetted into Amicon Ultra-0.5 mL centrifugal filters (MWCO 10,000, Merck Millipore, cat. # UFC501096) and spun (14,000 g, 15 min, 4 °C). The filtrate was then collected, weighed, and then transferred into UV-transparent 96-well plates. Its absorption at λ_{max} CoA = 259 nm was measured using a microplate reader (Infinite® M1000 Pro, Tecan Trading AG, Switzerland). Drug encapsulation was calculated by getting the ratio of the filtrate absorbance to that of the original (±)-C75-CoA solution added to form the micelle.

4.5 Cell cultures and treatments

Glioblastoma U87MG cell line (Merk Millipore, Sigma, Madrid, Spain) was cultured in DMEM (4.5 g/L glucose) supplemented with 10% FBS while murine hypothalamic neuronal cells GT1-7 (Merk Millipore, Sigma, Madrid, Spain) were cultured in DMEM (4.5 g/L glucose) supplemented with 10% FBS, 4 mM L-glutamine, 1% penicillin-streptomycin, and 1 mM sodium pyruvate at 37 °C in a humidified atmosphere of 95% air and 5% CO_2.

4.6 Cytotoxicity assays

In vitro cytotoxicity of etomoxir (ETO, Cayman, cat. # 11969) and free and micellar C75-CoA derivatives (racemic and enantiopures with CoA adduct) were evaluated against human GB cell lines and U87MG. The cells (3×10^4 cells / well) were seeded in a 96-well plate 24 h prior to the assay. The cells were incubated with the test solutions, and then viability was measured after 24, 48, and 72 h of exposure, by adding cell-counting kit-8 (CCK8) (Dojindo, cat. # CK04) and measuring the product absorbance at λ_{max} = 450 nm after 2 h using a microplate reader (Infinite® M1000 Pro, Tecan Trading AG, Switzerland).

4.7 Synthesis of Fluor-CoA and preparation of Fluor-CoA micelles

The synthetic procedure of Fluor-CoA was adopted from a previous protocol [55]. Briefly, 11.1 mg CoA sodium salt hydrate was dissolved in 100 µL 10 mM phosphate buffer pH 7.4. To this, 4.8 mg fluorescein-5-maleimide (TCI, cat. # F0810) in 900 µL DMF was added. The reaction mixture was stirred overnight at 30 °C. After which, benzene was added the resulting mixture, flash-frozen using liquid N_2 and then dried *in vacuo*. To confirm product formation, HPLC was performed [LC-2000 series, JASCO, Tokyo, Japan; C-18 RP-column (TSKgel ODS-100V 5µm particle size, 4.6 mm I.D. × 15 cm, TOSOH Bioscience, cat. # 21455), mobile phase 7:3

100 mM phosphate buffer pH 3/acetonitrile, flow rate 1.2 mL/minute, detection: UV absorption at λ_{max} CoA = 259 nm and λ_{max} fluorescein = 460 nm, fluorescence detection ($\lambda_{excitation}$ = 494 nm, $\lambda_{emission}$ = 521 nm)]. The HPLC peak passing all the detection criteria corresponds to the compound with both CoA and fluorescein moieties. ^{1}H NMR was recorded on a JEOL ECS 400 (400 MHz) spectrometer (JOEL Ltd., Tokyo Japan) and chemical shift was calculated as parts per million (ppm). Data was processed using MestReNova version 14.2.1-27684.

PEG-PAsp(DET) and Fluor-CoA solutions in 10 mM phosphate buffer pH 7.4 were then mixed in a 1:1 anion-to-cation ratio, vortexed, and then again filtered (0.22-μM) under sterile conditions.

4.8 Measurement of ATP levels

Measurement of ATP levels in parallel to cell viability assays were performed according to a previously reported procedure [38]. Produced ATP was quantified using a luminescence assay. Cells (2×10^5 cells/well) were seeded in a white, flat-bottom 96-well tissue culture plate 24 h prior to the assay. The cells were then incubated with ETO, C75-CoA, and C75-CoA micelle (0.5 mM) in bicarbonate-free DMEM (Sigma-Aldrich, cat. # D5030) supplemented with 2.5 mM glucose (Gibco, cat. # A2494001) and 275 nM oleate-BSA (Sigma-Aldrich, cat. # O3008) for 45 minutes in a separate incubator with 0% CO_2. The assay was done according to manufacturer protocol (CellTiter-Glo® Luminescent Cell Viability Assay, Promega, cat. # G9241). ATP was quantified using a calibration curve. Luminescence signal for 10s were measured in each well using GloMax® Multi Detection System (Promega Corp, Madison, Wisconsin).

The relative viability was determined using the Calcein AM assay. In parallel to the ATP measurements, cells (2×10^4 cells/well) were seeded in a white 96-well tissue culture plate 24 h prior to the assay. The cells were then incubated with ETO, C75-CoA, and C75-CoA micelle (1 mM) in bicarbonate-free DMEM (with 25 mM glucose and 6 mM glutamine) for 45 minutes in a separate incubator with 0% CO_2. The assay was then performed according to manufacturer protocol (Calcein AM; Invitrogen). Calcein AM was added to each well 30 min before measuring fluorescence intensity ($\lambda_{excitation}$ = 495 nm, $\lambda_{emission}$ = 515 nm) using a microplate reader (Infinite® M1000 Pro, Tecan Trading AG, Switzerland). Viability was normalized against non-treated cells.

4.9 Measurement of FAO

Palmitate oxidation to CO_2 and acid-soluble products (ASPs), essentially acyl-carnitine, Krebs cycle intermediates, and acetyl-CoA, were measured in U87 and GT1-7 cell lines grown in 12-well plates. Cells were treated with ETO, C75-CoA (racemic and enantiomers), and C75-CoA micelle (racemic and enantiomers) (1 mM) in DMEM (4.5 g/L glucose) for 45 minutes. On the day of the assay, cells were washed in KRBH-0.1% BSA, preincubated for 30 min at 37°C in KRBH-1% BSA. Cells were then incubated for 3 h at 37°C with fresh KRBH containing 2.5 mM glucose and 80 nM of labeled palmitate per well. Oxidation was measured as described [56] . The scintillation values were normalized to the protein content of each well and the result for CO_2 and ASPs are expressed as previously described [56] .

4.10 Confocal laser scanning microscopy (CLSM)

Confocal images were taken using an LSM880 confocal microscope (Carl Zeiss, Oberkochen, Germany) at a magnification of 5× using white light, 488- and 633-nm lasers for $\lambda_{excitation}$ of Fluor-CoA and NucSpot® 650, respectively. U87MG and GT1-7 cells (6×10^4 cells / well) were seeded in μ-slide 8-well chambered coverslip (ibidi, cat. # 80826) 24 h prior to observation. Cells were then incubated with 100.0 μL nanoparticle suspension in medium (0.25 mg Fluor-CoA micelle/mL containing 0.1 mg Fluor-CoA/mL) as well as NucSpot® 650 (Biotium, cat. # 40082) as nuclear stain (1 μL/mL suspension) and Verapamil HCl as efflux pump inhibitor (1 μL/mL suspension) for 1 h. Cells were then washed 2 × with PBS (–) before replacing medium with DMEM containing Trypan Blue (0.5 μL/mL) to quench fluorescent dyes attached on the cell surface.

4.11 Quantification of cellular uptake using FACS

U87MG and GT1-7 cells (3×10^5 cells / well) were seeded in 6-well plates 24 h prior to the assay. Cells were then incubated with nanoparticle suspension in medium (0.25 mg Fluor-CoA micelle/mL containing 0.1 mg Fluor-CoA/mL) with varying incubation times (1, 3, and 6 h). The cell suspension was washed twice with 1 mL PBS (–) and then incubated with 300 μL Accutase® Cell Detachment Solution (Innovative Cell Technologies, San Diego, California) for 3 minutes at 37 °C. The cells were collected by adding 1 mL PBS (–), transferring to a 25-

mL plastic tube, and then spinning at 300 g for 5 mins at 4 °C. They were further washed twice with PBS (–) and twice with 2% FBS in PBS (–). After the final washing, they were resuspended in 500 μL of 1 μg/mL DAPI in 2% FBS in PBS (–) to stain live cells, then passed through a cell strainer and kept on ice. Mean fluorescence intensity and percentage of Fluor-CoA+ cells in FITC channel were measured by flow cytometry (BD LSRFortessa™ Flow Cytometer, BD Biosciences, San Jose, California) using FSC and SSC detection to gate out debris, and the UV (355 nm) and blue lasers (488 nm) for the detection of DAPI and Fluor-CoA, respectively. Data analysis was performed using FlowJo software (BD Biosciences, San Jose, California).

4.12 Spheroid culture and uptake measurement

For spheroid culture, cell suspensions (50 μL) were seeded into each well (1×10^3 cells/well) of a low-adhesion Prime Surface™ 96-well U-bottom plate (Sumitomo Bakelite Co., Japan) and incubated for 3 d. The spheroids were then incubated with Fluor-CoA free dye or micelle suspension (50 μL) in medium (final concentration: 0.25 mg Fluor-CoA micelle/mL containing 0.1 mg Fluor-CoA/mL) for 3 h. After which they were harvested using a pipette and collected into a 25-mL plastic tube. Washing and analysis were performed as above.

For confocal imaging, the spheroids were also incubated with NucSpot® 650 (Biotium, cat. # 40082) as nuclear stain (1 μL/mL suspension) and Verapamil HCl as efflux pump inhibitor (1 μL/mL suspension) in addition to Fluor-CoA free dye or micelle suspension. After 3 h, they were then harvested using a pipette and collected into a 25-mL plastic tube. The spheroids were collected by centrifugation at 700 rpm for 3 mins at 4 °C and washed twice with PBS (–) before fixing with 4% paraformaldehyde for 30 mins. After fixing, the spheroids were further washed with PBS (–) before mounting with 90% glycerol in a μ-slide 8-well chambered coverslip (ibidi, cat. # 80826). Images were taken with LSM880 confocal microscope (Carl Zeiss, Oberkochen, Germany) at a magnification of 1.2× using white light, 488- and 633-nm lasers for $\lambda_{excitation}$ of Fluor-CoA and NucSpot® 650, respectively. Z-stack images were taken at 15-μm intervals for U87MG and at 10-μm intervals for GT1-7. Image analysis was done using Zeiss Zen software, including measurement of spheroid diameters and radial fluorescence profile.

4.13 Statistical analysis

Data are expressed as means ± SD of assays performed at least triplicates. Several statistical analyses were performed using GraphPad version 9: (1) statistical significances were determined Student's t-test (column analysis), one-way ANOVA with Tukey's post-hoc (grouped analysis), or two-way ANOVA and (2) relationships between variables were analyzed using linear and non-linear regression using the same software.

AUTHOR CONTRIBUTIONS

WP – Investigation (polymer synthesis, micelle preparation and characterization, biochemical assays, and cellular internalization), Formal analysis, Methodology, Visualization, and Writing - original draft preparation; JGC – Investigation (drug synthesis and biochemical assays), Formal analysis, Visualization, and Writing - original draft preparation; XA – Investigation (drug synthesis), Methodology, and Writing - original draft preparation; SZ – Investigation (biochemical assays) and Visualization; SF – Investigation (polymer synthesis) and Methodology; JG – Investigation (drug synthesis) and Methodology; YM – Investigation (micelle characterization) and Formal analysis; DS, LH, HK, and NC – Resources and Critical review; KK – Supervision, Funding acquisition, and Critical review; RR and SQ – Conceptualization, Funding acquisition, Methodology, Project administration, Supervision, and Writing - original draft preparation. All authors contributed to the review and editing of the manuscript.

ACKNOWLEDGEMENTS

This project was financially supported by the Joint Bilateral Project Japan-Spain (PCI2018-092997 to RR)/Agencia Estatal de Investigación (AEI) and (20jm0210059h0003 to SQ)/ Agency for Medical Research and Development (AMED), the Japan Society for Promotion of Science (JSPS) Bilateral Joint Research Projects (JPJSBP120209938 to SQ), and the Center of Innovation (COI) Program (JPMJCE1305) from Japan Science and Technology Agency (JST). This study was also supported by the Ministry of Spain (MINECO) (SAF2017-83813-C3-3-R to NC and RR-R; SAF2017-83813-C3-1-R to DS and LH co-funded by the ERDF), the Centro de Investigación Biomédica en Red de Fisiopatología de la Obesidad y la Nutrición (CIBEROBN) (Grant CB06/03/0001 to DS), the Government of Catalonia (2017SGR278 to DS), and the Fundació La Marató de TV3 (201627-30 to DS). We thank Dr. Xueying Liu and Dr. Kazuko Toh for their guidance in confocal microscopy, Ms. Johanna Elter for their

assistance in flow cytometry, and Dr. Anjaneyulu Dirisala for the helpful discussion on cationic polymers. The authors have no other relevant affiliations or financial involvement with any organization or entity with a financial interest in or financial conflict with the subject matter or materials discussed in the manuscript apart from those disclosed.

REFERENCES

1 K. D. Bruce, A. Zsombok and R. H. Eckel, *Front. Endocrinol. (Lausanne).*, 2017, **8**, 1–11.
2 J. A. Hamilton, C. J. Hillard, A. A. Spector and P. A. Watkins, in *Journal of Molecular Neuroscience*, Springer, 2007, vol. 33, pp. 2–11.
3 E. Currie, A. Schulze, R. Zechner, T. C. Walther and R. V. Farese, *Cell Metab.*, 2013, **18**, 153–161.
4 N. Casals, V. Zammit, L. Herrero, R. Fadó, R. Rodríguez-Rodríguez and D. Serra, *Prog. Lipid Res.*, 2016, **61**, 134–148.
5 R. Fadó, R. Rodríguez-Rodríguez and N. Casals, *Prog. Lipid Res.*, 2021, 81.
6 I. R. Schlaepfer and M. Joshi, *Endocrinol. (United States)*, 2020, 161.
7 A. Pocai, T. K. T. Lam, S. Obici, R. Gutierrez-Juarez, E. D. Muse, A. Arduini and L. Rossetti, *J. Clin. Invest.*, 2006, **116**, 1081–1091.
8 K. Makowski, P. Mera, D. Paredes, L. Herrero, X. Ariza, G. Asins, F. G. Hegardt, J. García and D. Serra, *Chirality*, 2013, **25**, 281–287.
9 S. Obici, Z. Feng, A. Arduini, R. Conti and L. Rossetti, *Nat. Med.*, 2003, **9**, 756–761.
10 R. Lage, M. J. Vázquez, L. Varela, A. K. Saha, A. Vidal-Puig, R. Nogueiras, C. Diéguez and M. López, *FASEB J.*, 2010, **24**, 2670–2679.
11 A. Cirillo, A. Di Salle, O. Petillo, M. A. B. Melone, G. Grimaldi, A. Bellotti, G. Torelli, M. S. De' Santi, G. Cantatore, A. Marinelli, U. Galderisi and G. Peluso, *Cancer Biol. Ther.*, 2014, **15**, 735–41.
12 J. Sperry, M. C. Condro, L. Guo, D. Braas, N. Vanderveer-Harris, K. K. O. Kim, W. B. Pope, A. S. Divakaruni, A. Lai, H. Christofk, M. G. Castro, P. R. Lowenstein, J. E. Le Belle and H. I. Kornblum, *iScience*, 2020, **23**, 101453.
13 G. Petővári, T. Dankó, I. Krencz, Z. Hujber, H. Rajnai, E. Vetlényi, R. Raffay, J. Pápay, A. Jeney and A. Sebestyén, *Pathol. Oncol. Res.*, 2020, **26**, 23–33.
14 K. Zaugg, Y. Yao, P. T. Reilly, K. Kannan, R. Kiarash, J. Mason, P. Huang, S. K. Sawyer, B. Fuerth, B. Faubert, T. Kalliomäki, A. Elia, X. Luo, V. Nadeem, D. Bungard, S. Yalavarthi, J. D. Growney, A. Wakeham, Y. Moolani, J. Silvester, A. Y. Ten, W. Bakker, K. Tsuchihara, S. L. Berger, R. P. Hill, R. G. Jones, M. Tsao, M. O. Robinson, C. B. Thompson, G. Pan and T. W. Mak, *Genes Dev.*, 2011, **25**, 1041–51.
15 S. M. Ceccarelli, O. Chomienne, M. Gubler and A. Arduini, *J. Med. Chem.*, 2011, **54**, 3109–3152.
16 A. Bentebibel, D. Sebastián, L. Herrero, E. López-Viñas, D. Serra, G. Asins, A. Paulino Gómez-Puertas, Fausto G. Hegardt, P. Gómez-Puertas and F. G. Hegardt, *Biochemistry*, 2006, **45**, 4339–4350.
17 P. Mera, A. Bentebibel, E. López-Viñas, A. G. Cordente, C. Gurunathan, D. Sebastián, I. Vázquez, L. Herrero, X. Ariza, P. Gómez-Puertas, G. Asins, D. Serra, J. García and F. G. Hegardt, *Biochem. Pharmacol.*, 2009, **77**, 1084–1095.
18 R. Conti, E. Mannucci, P. Pessotto, E. Tassoni, P. Carminati, F. Giannessi and A. Arduini, *Diabetes*, 2011, **60**, 644–651.

19 R. S. O'Connor, L. Guo, S. Ghassemi, N. W. Snyder, A. J. Worth, L. Weng, Y. Kam, B. Philipson, S. Trefely, S. Nunez-Cruz, I. A. Blair, C. H. June and M. C. Milone, *Sci. Rep.*, 2018, **8**, 1–9.

20 K. Makowski, P. Mera, J. Ariza, D. Serra, J. Garcia, L. Herrero, M. López and A. Venegas, *Rev. Bionatura*, 2019, **4**, 1–5.

21 A. Gautier and M. J. Hinner, *Site-Specific Protein Labeling Methods Protoc.*, 2015, 1–267.

22 M. C. Cheng, X. H. Qiang and C. M. Du, *Chinese Sci. Bull.*, 2013, **58**, 1256–1261.

23 H. Cabral, K. Miyata, K. Osada and K. Kataoka, *Chem. Rev.*, 2018, **118**, 6844–6892.

24 A. Harada and K. Kataoka, *Polym. J.*, 2018, **50**, 95–100.

25 S. Quader and K. Kataoka, *Mol. Ther.*, 2017, **25**, 1501–1513.

26 C. Wang, Q. Chen, Z. Wang and X. Zhang, *Angew. Chemie - Int. Ed.*, 2010, **49**, 8612–8615.

27 H. Uchida, K. Miyata, M. Oba, T. Ishii, T. Suma, K. Itaka, N. Nishiyama and K. Kataoka, *J. Am. Chem. Soc.*, 2011, **133**, 15524–15532.

28 H. Uchida, K. Itaka, T. Nomoto, T. Ishii, T. Suma, M. Ikegami, K. Miyata, M. Oba, N. Nishiyama and K. Kataoka, *J. Am. Chem. Soc.*, 2014, **136**, 12396–12405.

29 C. Y. Lin, F. Perche, M. Ikegami, S. Uchida, K. Kataoka and K. Itaka, *J. Control. Release*, 2016, **235**, 268–275.

30 S. T. Crowley, Y. Fukushima, S. Uchida, K. Kataoka and K. Itaka, *Mol. Ther. - Nucleic Acids*, 2019, **17**, 465–476.

31 H. Helmbrecht, A. Joseph, M. McKenna, M. Zhang and E. Nance, *Curr. Opin. Chem. Eng.*, 2020, **30**, 112–119.

32 E. A. Nance, G. F. Woodworth, K. A. Sailor, T.-Y. Shih, Q. Xu, G. Swaminathan, D. Xiang, C. Eberhart and J. Hanes, *Sci. Transl. Med.*, 2012, **4**, 149ra119-149ra119.

33 E. Nance, K. Timbie, G. W. Miller, J. Song, C. Louttit, A. L. Klibanov, T. Y. Shih, G. Swaminathan, R. J. Tamargo, G. F. Woodworth, J. Hanes and R. J. Price, *J. Control. Release*, 2014, **189**, 123–132.

34 A. G. Godin, J. A. Varela, Z. Gao, N. Danné, J. P. Dupuis, B. Lounis, L. Groc and L. Cognet, *Nat. Nanotechnol.*, 2017, **12**, 238–243.

35 C. Paviolo, F. N. Soria, J. S. Ferreira, A. Lee, L. Groc, E. Bezard and L. Cognet, *Methods*, 2020, **174**, 91–99.

36 C. Curtis, M. McKenna, H. Pontes, D. Toghani, A. Choe and E. Nance, *Nanoscale*, 2019, **11**, 22515–22530.

37 Y. Ma, S. M. Temkin, A. M. Hawkridge, C. Guo, W. Wang, X. Y. Wang and X. Fang, *Fatty acid oxidation: An emerging facet of metabolic transformation in cancer*, Elsevier B.V., 2018, vol. 435.

38 L. S. Pike, A. L. Smift, N. J. Croteau, D. A. Ferrick and M. Wu, *Biochim. Biophys. Acta - Bioenerg.*, 2011, **1807**, 726–734.

39 M. Allen, M. Bjerke, H. Edlund, S. Nelander and B. Westermark, *Sci. Transl. Med.*, 2016, **8**, 354re3-354re3.

40 S. Kant, P. Kesarwani, A. Prabhu, S. F. Graham, K. L. Buelow, I. Nakano and P. Chinnaiyan, *Cell Death Dis.*, 2020, **11**, 1–13.

41 B. Juraszek, J. Czarnecka-Herok and K. A. Nałęcz, *J. Neurochem.*, 2020, jnc.15124.

42 A. S. Divakaruni, W. Y. Hsieh, L. Minarrieta, T. N. Duong, K. K. O. Kim, B. R. Desousa, A. Y. Andreyev, C. E. Bowman, K. Caradonna, B. P. Dranka, D. A. Ferrick, M. Liesa, L. Stiles, G. W. Rogers, D. Braas, T. P. Ciaraldi, M. J. Wolfgang, T. Sparwasser, L. Berod, S. J. Bensinger and A. N. Murphy, *Cell Metab.*, 2018, **28**, 490-503.e7.

43 Y. Arai, H. Ishii, M. Kobayashi and H. Ozawa, *J. Physiol. Sci.*, 2017, **67**, 313–323.

44 B. Taïb, K. Bouyakdan, C. Hryhorczuk, D. Rodaros, S. Fulton and T. Alquier, *J. Biol.*

Chem., 2013, **288**, 37216–37229.
45 A. C. Hunter, *Adv. Drug Deliv. Rev.*, 2006, 58, 1523–1531.
46 S. J. Choi, F. Kim, M. W. Schwartz and B. E. Wisse, *Am. J. Physiol. Metab.*, 2010, **298**, E1122–E1130.
47 J. F. Mir, S. Zagmutt, M. P. Lichtenstein, J. García-Villoria, M. Weber, A. Gracia, G. Fabriàs, J. Casas, M. López, N. Casals, A. Ribes, C. Suñol, L. Herrero and D. Serra, *Mol. Neurobiol.*, 2018, **55**, 7216–7228.
48 H. Lin, S. Patel, V. S. Affeck, I. Wilson, D. M. Turnbull, A. R. Joshi, R. Maxwell, E. A. Stoll, V. S. Affleck, I. Wilson, D. M. Turnbull, A. R. Joshi, R. Maxwell and E. A. Stoll, *Neuro. Oncol.*, 2017, **19**, 43–54.
49 L. Mo, L. Hou, D. Guo, X. Xiao, P. Mao and X. Yang, *Int. J. Pharm.*, 2012, **436**, 815–824.
50 J. M. Rabanel, P. A. Piec, S. Landri, S. A. Patten and C. Ramassamy, *J. Control. Release*, 2020, **328**, 679–695.
51 R. Vadivelu, H. Kamble, M. Shiddiky and N.-T. Nguyen, *Micromachines*, 2017, **8**, 94.
52 A. Tchoryk, V. Taresco, R. H. Argent, M. Ashford, P. R. Gellert, S. Stolnik, A. Grabowska and M. C. Garnett, *Bioconjug. Chem.*, 2019, **30**, 1371–1384.
53 J. Garcia-Chica, W. K. D. Paraiso, S. Tanabe, D. Serra, L. Herrero, N. Casals, J. Garcia, X. Ariza, S. Quader and R. Rodriguez-Rodriguez, *Nanomedicine (Lond).*, 2020, **15**, 1617–1636.
54 S. Quader, H. Cabral, Y. Mochida, T. Ishii, X. Liu, K. Toh, H. Kinoh, Y. Miura, N. Nishiyama and K. Kataoka, *J. Control. Release*, 2014, **188**, 67–77.
55 New England Biolabs Inc., Reaction Conditions for Chemical Coupling with CoA-SH (S9352S), https://international.neb.com/protocols/2012/08/09/reaction-conditions-for-chemical-coupling-with-coa-sh-s9352s, (accessed 11 May 2020).
56 M. I. Malandrino, R. Fucho, M. Weber, M. Calderon-Dominguez, J. F. Mir, L. Valcarcel, X. Escoté, M. Gómez-Serrano, B. Peral, L. Salvadó, S. Fernández-Veledo, N. Casals, M. Vázquez-Carrera, F. Villarroya, J. J. Vendrell, D. Serra and L. Herrero, *Am. J. Physiol. - Endocrinol. Metab.*, 2015, **308**, E756–E769.